Cell Reports
Physical Science

CellPress
OPEN ACCESS

Article

# Atomically dispersed S-Fe-$N_4$ for fast kinetics sodium-sulfur batteries via a dual function mechanism

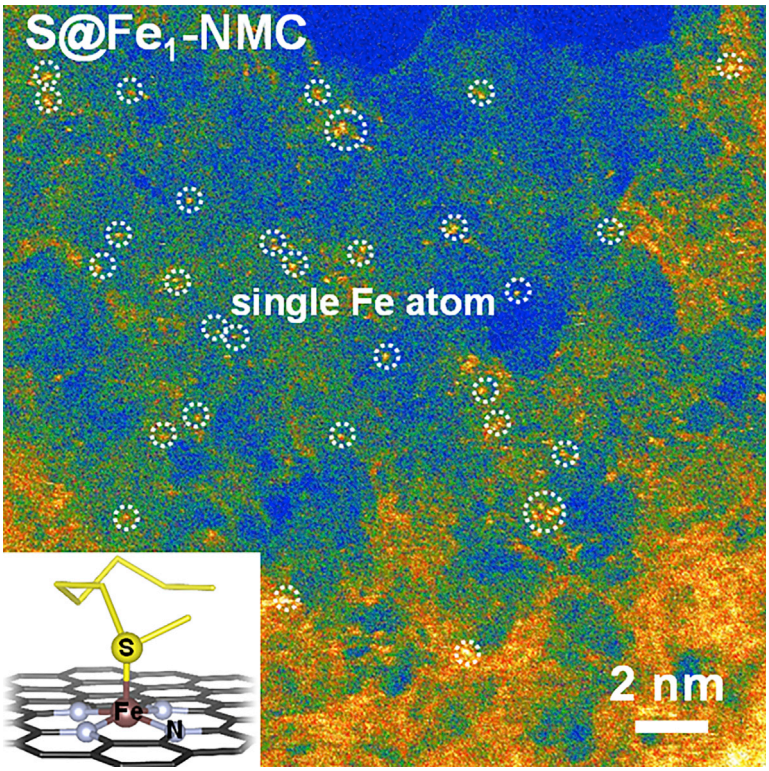


Zhang et al. report that atomically dispersed Fe-$N_4$ sites can modify sulfur's electronic structure and enhance the activity of sulfur. They can boost the performance toward Na-S batteries by a dual function mechanism, accelerating $Na^+$ ion diffusion and enhancing the kinetic conversion of polysulfides by weakening their S-S bonds.

Bin-Wei Zhang, Shunning Li, Hui-Ling Yang, ..., Shu-Lei Chou, Hua-Kun Liu, Shi-Xue Dou

liuyue.cao@sydney.edu.au (L.C.)
yunxiao@uow.edu.au (Y.-X.W.)
panfeng@pkusz.edu.cn (F.P.)
shulei@uow.edu.au (S.-L.C.)

## Highlights

Atomically dispersed Fe-$N_4$ sites for sulfur hosts

The fabricated cathode delivers a high reversible capacity

A dual function mechanism is proposed

Zhang et al., Cell Reports Physical Science 2, 100531
August 18, 2021 
https://doi.org/10.1016/j.xcrp.2021.100531

Cell Reports
Physical Science

CellPress
OPEN ACCESS

Article

# Atomically dispersed S-Fe-$N_4$ for fast kinetics sodium-sulfur batteries via a dual function mechanism

Bin-Wei Zhang,[1,2,7] Shunning Li,[3,7] Hui-Ling Yang,[2,7] Xianhui Liang,[3] Wei-Hong Lai,[2] Shenlong Zhao,[4] Juncai Dong,[5] Sheng-Qi Chu,[5] Qin-Fen Gu,[6] Ji Liang,[2] Yi Du,[2] Xun Xu,[2] Liuyue Cao,[1,4,*] Yun-Xiao Wang,[2,*] Feng Pan,[3,*] Shu-Lei Chou,[1,2,8,*] Hua-Kun Liu,[2] and Shi-Xue Dou[2]

## SUMMARY

**Room-temperature sodium-sulfur batteries have significant potential for large-scale applications due to the low cost and high energy density of both sulfur and sodium. Nevertheless, the insulating nature of sulfur and the shuttle effect are impeding their practical application. Here we report that dispersed single-atom Fe sites anchored on a nitrogen-doped carbon matrix present an atomic-level strategy for the development of sulfur hosts. The electronic structure of sulfur is modified by the atomically dispersed Fe-$N_4$ sites, which can transfer the electron to sulfur, thereby enhancing its reactivity. The S@$Fe_1$-NMC cathode delivers a high reversible capacity of 1,650 mAh $g^{-1}$ initially and 540 mAh $g^{-1}$ after 500 cycles at 100 mA $g^{-1}$. A dual function mechanism is observed on S-Fe-$N_4$ sites, which can activate the polysulfides by weakening the S-S bonds and accelerate $Na^+$ diffusion into Na-poor regions to engender a high driving force for $Na_2S_x$ decomposition, thus inhibiting the shuttle effect.**

## INTRODUCTION

As one of the spotlights of worldwide research on energy storage systems, metal-sulfur (M-S) batteries have shown tremendous promise for applications in electric vehicles and smart grids because of the exceptionally high theoretical capacity (1,672 mAh $g^{-1}$) of the sulfur electrode.[1–3] Furthermore, the sulfur cathode can be coupled with various kinds of metal anodes for high-energy-density M-S batteries (~350 W h $kg^{-1}$, based on devices).[4–8] Among these M-S batteries, room-temperature sodium-sulfur (RT-Na/S) batteries have attracted significant attention due to the low cost and abundance of both sodium and sulfur.[9–12] Nevertheless, the insulating nature and low reactivity of sulfur suppress the complete reduction of $Na_2S_x$ ($2 \leq x \leq 8$) to the final product $Na_2S$, leading to a serious limitation in reversible capacity.[13–15] The shuttle effect, arising from the dissolution of intermediate metal polysulfides, poses an additional challenge for the practical application of Na-S batteries.[16,17] This phenomenon will lead to the loss of active materials and rapid capacity decay during cycling. To solve these problems, various carbon materials,[18–20] metal nanoclusters,[21–23] and sulfides[24,25] have been introduced as novel S hosts to enhance the reactivity between sodium and sulfur. In addition, various strategies, such as confinement of polysulfides[26–28] and modified separators,[29,30] have been developed to trap the polysulfides so as to relieve the shuttle effect. These methods could enhance the performance of RT-Na/S batteries, but systematic investigation of the kinetic conversion of sodium polysulfides remains limited. Moreover, to our knowledge, the effect of Na ion diffusion on the electrochemical performance of

[1]Institute for Carbon Neutralization, College of Chemistry and Materials Engineering, Wenzhou University, Wenzhou, Zhejiang 325035, People's Republic of China

[2]Institute for Superconducting and Electronic Materials, Australian Institute of Innovative Materials, University of Wollongong, Innovation Campus, Squires Way, North Wollongong, NSW 2500, Australia

[3]School of Advanced Materials, Peking University, Shenzhen Graduate School, Shenzhen 518055, People's Republic of China

[4]The University of Sydney, School of Chemical and Biomolecular Engineering, Sydney, NSW 2006, Australia

[5]Beijing Synchrotron Radiation Facility, Institute of High Energy Physics, Chinese Academy of Sciences, Beijing 100049, People's Republic of China

[6]Australian Synchrotron, 800 Blackburn Road, Clayton, VIC 3168, Australia

[7]These authors contributed equally

[8]Lead contact

*Correspondence:
liuyue.cao@sydney.edu.au (L.C.),
yunxiao@uow.edu.au (Y.-X.W.),
panfeng@pkusz.edu.cn (F.P.),
shulei@uow.edu.au (S.-L.C.)

https://doi.org/10.1016/j.xcrp.2021.100531

RT-Na/S batteries, which is intimately associated with the conversion of sodium polysulfides, has never been explored. The complexity of the conversion reaction makes the rational design of the desired sulfur cathode a challenge. Therefore, a comprehensive understanding of the sodiation mechanism at the atomic level is urgently required.

Single-atom catalysts (SACs) with well-defined metal centers atomically dispersed on a solid matrix usually have a unique electronic structure and maximum atom utilization.[31–34] Because of these merits, SACs have been identified as efficient catalysts in electrochemical energy conversion and storage.[35–40] For example, Qiu et al.[41] reported that iron (Fe)-$N_2$ sites could trap lithium (Li) polysulfides to accelerate its redox conversion and reduce the decomposition energy barrier of $Li_2S$. Single Co atoms have been anchored on nitrogen-doped graphene (NG) as an electrocatalyst to facilitate the formation of $Li_2S$ for Li-S batteries.[42] Nickel (Ni)-$N_4$ on NG was employed to modify the separate components, which could form $S_x^{2-}$-Ni-nitrogen (N) bonds, thus trapping lithium polysulfides during the charge/discharge process.[43] It is therefore interesting to manipulate the Na-S chemistry by introducing SACs onto S hosts, which is expected to improve the reactivity of sulfur and serve as a model system to investigate the kinetic conversion of reaction intermediates in RT/Na-S batteries.

Here, we report a novel sulfur host with single Fe atoms anchored on nitrogen-doped mesoporous hollow carbon (S@$Fe_1$-NMC), which marries the advantages of the catalytically active SACs and the rigid carbon framework for sulfur encapsulation. According to the experimental and density functional theory (DFT) calculation results, we demonstrate that the Fe-$N_4$ sites can effectively induce chemical adsorption of sulfur via electron ($e^-$) transfer. S@$Fe_1$-NMC delivers an unprecedented initial reversible capacity of 1,650 mAh $g^{-1}$ and retains a high reversible capacity of 540 mAh $g^{-1}$, despite going through 500 cycles at 0.1 A $g^{-1}$. Good agreement between density functional theory computations and electrochemical results underscores that these S-Fe-$N_4$ sites can accelerate $Na^+$ diffusion and boost the kinetic conversion of intermediates in RT-Na/S batteries, inhibiting the shuttle effect. The proposed dual function mechanistic insight into the kinetic conversion of the polysulfides can apply generally to the investigation of high-performance, practical RT-Na/S batteries.

## RESULTS AND DISCUSSION

### Dual function mechanism

The most widely investigated Fe-pyridine-$N_4$ configuration, in which an isolated transition metal atom occupies a di-vacancy in graphene and binds to four pyridinic N,[44] was used to unravel the atomic level mechanisms of RT/Na-S batteries. To simplify the notation, we define one of the S atoms at the end of a $S_x$ chain as the $S^{(1)}$ atom, the atom next to it as $S^{(2)}$, and so on (Figure 1A). The electron density difference plots for $Na_2S_8$ adsorbed on Fe-pyridine-$N_4$ are presented in Figure 1B. $Na_2S_8$ adsorbed on graphitic N and pyridinic $N_4$ are taken as references. Pronounced electron redistribution takes place in the area between $Na_2S_8$ and Fe-pyridine-$N_4$, whereas little evidence of electron transfer is found between $Na_2S_8$ and N-doped carbon, indicating strong interaction between S atoms and Fe ions. This result, combined with the observation that the distance of S atoms to Fe-pyridine-$N_4$ (~2.2 Å) is shorter than the distance to graphitic N or pyridinic $N_4$ (>3 Å), provides strong evidence that Fe plays a critical role in chemically binding the $S_x$ chains and altering their electronic structures. This can be substantiated by the increase in S-S bond length shown in Figure 1C. For $Na_2S_x$ ($4 \leq x \leq 8$), the adsorption of $S^{(i)}$ atoms

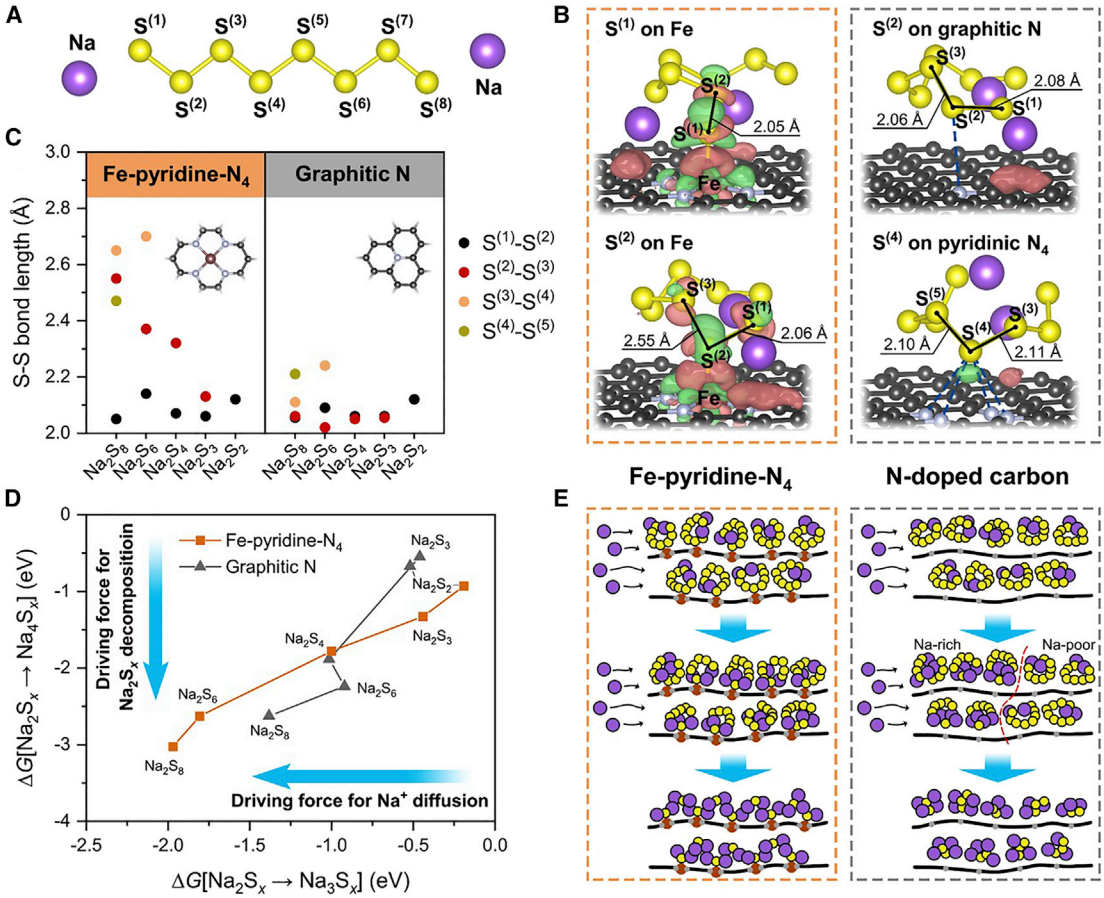


**Figure 1. DFT calculations**

(A) Notation of sulfur atoms on a $Na_2S_8$ chain.

(B) Electron density difference map with isosurfaces of 0.015 $Å^{-1}$ for $Na_2S_8$ adsorbed on Fe, Fe-pyridine-$N_4$, graphitic N, and pyridinic $N_4$. The red and green contours represent charge accumulation and depletion, respectively.

(C) $S^{(i)}$-$S^{(i+1)}$ bond lengths when $S^{(i)}$ is on top of a catalytic center.

(D) Reaction energies of $Na_2S_x$ with one $Na^+/e^-$ pair, $\Delta G[Na_2S_x \rightarrow Na_3S_x]$, versus those with two $Na^+/e^-$ pairs, $\Delta G[Na_2S_x \rightarrow Na_4S_x]$.

(E) Structural evolution during the discharge of S@$Fe_1$-NMC and S@NMC cathodes. Color code: yellow, S; purple, Na; black, C; gray, N; brown, Fe.

on Fe-pyridine-$N_4$ will lead to a significant increase in $S^{(i)}$-$S^{(i+1)}$ bond length (originally ~2.06 Å), except for the case of $S^{(1)}$, which probably results from the unpaired electron on the $S^{(1)}$ atom. The elongated S-S bond suggests lower energy of the antibonding orbitals and a higher propensity for the $S_x$ chain to accept electrons, which will benefit the sodiation process. In addition, the Fe-S interaction is characteristic of net-electron transfer from Fe to S atoms, the amount of which is nearly the same for different $Na_2S_x$ adsorption configurations (Table S1).

We calculated the Gibbs free reaction (ΔG) energies of $Na_2S_x$ with one $Na^+/e^-$ pair yielding $Na_3S_x$ and two $Na^+/e^-$ pairs yielding $Na_4S_x$ (or $Na_2S_y$ + $Na_2S_{x-y}$, $0 < y < x$), denoted as $\Delta G[Na_2S_x \rightarrow Na_3S_x]$ and $\Delta G[Na_2S_x \rightarrow Na_4S_x]$, respectively. The geometric structures of all configurations are provided in Figures S1–S12. The reaction energy is averaged over all adsorption configurations for each polysulfide. A more negative ΔG $[Na_2S_x \rightarrow Na_3S_x]$ would mean that a larger energy gain is expected when $Na_2S_x$ accepts the first $Na^+/e^-$ pair; in other words, there is a more exergonic driving force for $Na^+$ ions diffusing into a Na-poor region and binding to a Na-deficient $Na_2S_x$ chain. However, because $Na_4S_x$ can potentially decompose into $Na_2S_y$ and $Na_2S_{x-y}$, a more

negative $\Delta G[Na_2S_x \rightarrow Na_4S_x]$ would indicate a higher thermodynamic driving force for $Na_2S_x$ decomposition after receiving two $Na^+/e^-$ pairs. As shown in Figure 1D, for long-chain polysulfides ($4 \leq x \leq 8$), Fe-pyridine-$N_4$ can enhance $Na^+$ diffusivity compared with graphitic N, whereas for short-chain polysulfides ($2 \leq x \leq 3$), Fe-pyridine-$N_4$ can help decompose $Na_2S_x$. Actually, spontaneous S-S bond cleavage is observed for all polysulfides after the first or second elementary sodiation step on Fe-pyridine-$N_4$. In contrast, when adsorbed on N-doped carbon, $Na_2S_3$ and $Na_2S_2$ remain intact, even after adding the second $Na^+/e^-$ pair (Figures S8 and S10). Moreover, the stronger binding of polysulfides on Fe-pyridine-$N_4$ than on graphitic N (Figure S11) demonstrates the benefit of Fe-pyridine-$N_4$ in alleviating the shuttle effect.

The dual function mechanism of Fe-pyridine-$N_4$ for boosting the electrochemical performance of Na/S cells can be visualized in Figures 1D and 1E. The Fe-pyridine-$N_4$ cathode facilitates facile Na diffusion into Na-poor regions and high conversion efficiency of the intermediates to the final product $Na_2S$, whereas distinct phase separation between Na-rich and Na-poor regions would likely occur in the N-doped carbon cathode because of the insufficient driving force for even distribution of the Na ions. This feature in the N-doped carbon, together with the insusceptibility of short-chain polysulfides to decomposition, could explain the reasons for low-capacity utilization of traditional Na/S cells.

### S-Fe-$N_4$ site design and fabrication

To verify the preceding theoretical analysis, a new sulfur host consisting of a single Fe atom anchored on N-doped mesoporous hollow carbon (NMC) has been synthesized. The nitrogen adsorption/desorption isotherm and pore size distribution of NMC (Figure S13) demonstrate that NMC has a high surface area of 715 $m^2/g$ and a mesoporous structure with average pore width of ~4.3 nm. Scanning electron microscope (SEM) images of NMC (Figure S14) showed its nanosphere structure and its size are homogeneous. $Fe_1$-NMC was prepared via acid leaching of Fe nanoparticles, and then single Fe atoms were anchored by the nitrogen functional. SEM images of $Fe_1$-NMC in Figure S15 indicated that after loading single Fe atoms, it could maintain its nanosphere structure. The Raman spectra of the two samples in Figure S16A showed that the $I_D/I_G$ of $Fe_1$-NMC is close to that of NMC, also indicating the highly stable nanosphere structure in NMC. The X-ray diffraction (XRD) pattern in Figure S15B didn't present any Fe bulk signal, suggesting it is atomically dispersed. S was loaded into $Fe_1$-NMC, which sealed both in a quartz ampoule that was maintained at 300°C for 12 h, as illustrated in Figure 2A. The Fe-$N_4$ sites in S@$Fe_1$-NMC are expected to enhance Na ion diffusion and improve the kinetic conversion of reaction intermediates, inhibiting the shuttle effect. High-angle annular dark field (HAADF)-scanning transmission electron microscopy (STEM) images and the corresponding elemental mapping of S@$Fe_1$-NMC (Figures 2B–2I) demonstrated that sulfur had been successfully dispersed on the carbon walls, and no obvious Fe nanoparticles could be found. The carbon layer (Figures 2C and 2D) in the carbon wall in NMC is about 3.4 Å, corresponding to the graphene layer in graphite[45]; the average size of the wall thickness is 4.9 ± 1.1 nm (Figure S17). The carbon layer and the hollow nanosphere structure will enhance the conductivity of S@$Fe_1$-NMC and simultaneously provide more space to store sulfur. After loading sulfur, the single Fe atoms remain atomically dispersed (Figures 2D and 2E; Figure S18), indicating that sulfur atoms are likely to bind to single Fe atoms. The pore size distributions of $Fe_1$-NMC and S@$Fe_1$-NMC are shown in Figure S19. The Brunauer–Emmett–Teller (BET) surface area is decreased from 327.3790 $m^2/g$ ($Fe_1$-NMC) to 10.5317 $m^2/g$ (S@$Fe_1$-NMC). It also could be clearly seen that the <3 nm pores disappeared after loading S. These results suggest that sulfur has been successfully loaded on the pores of NMC.

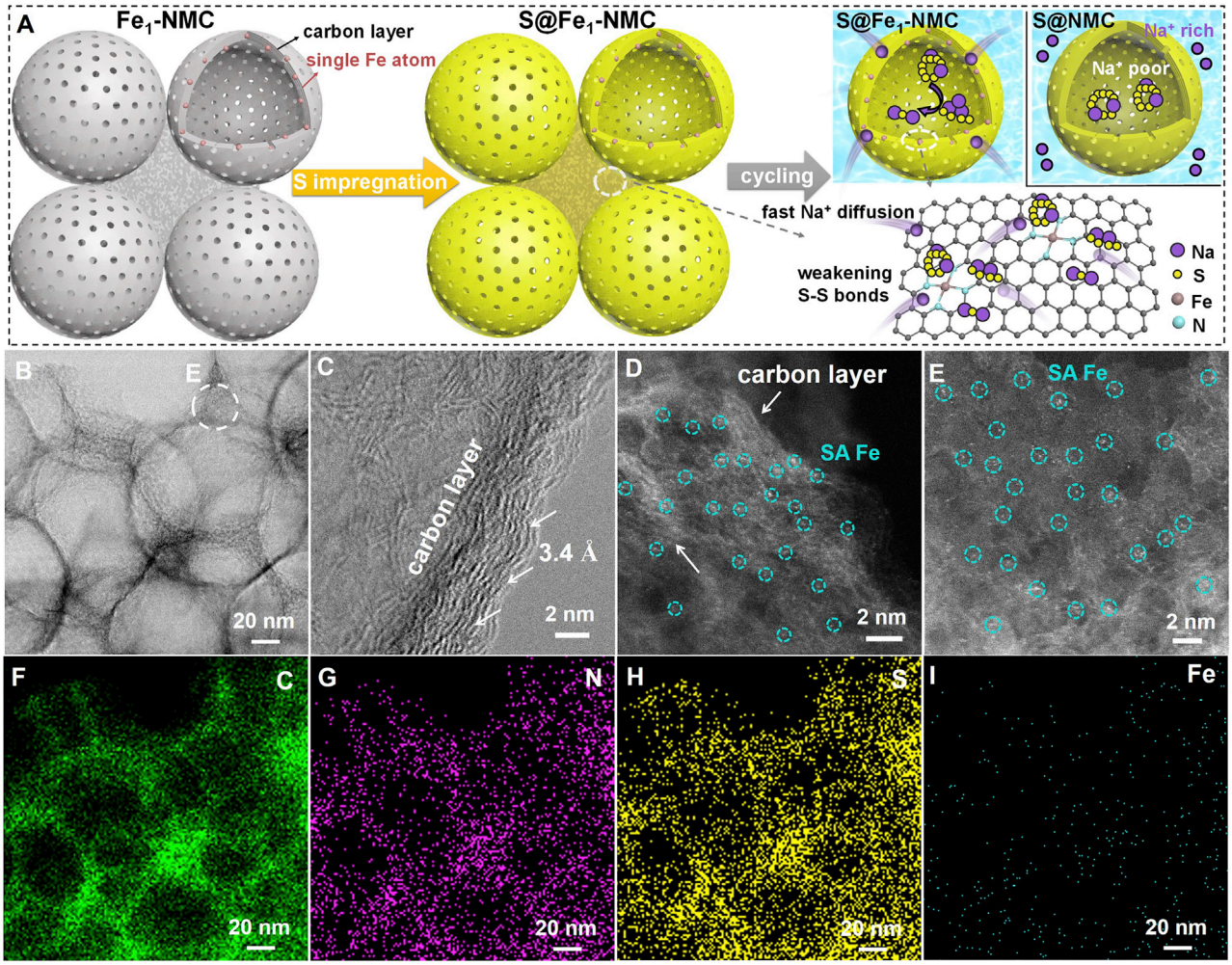


**Figure 2. Electron microscope images of S@$Fe_1$-NMC**

(A) Schematic illustration of synthesis of S@$Fe_1$-NMC and electrode reaction mechanism of S@NMC and S@$Fe_1$-NMC.

(B–E) TEM images and high-resolution (HR) STEM images of S@$Fe_1$-NMC.

(F–I) Corresponding elemental mapping of S@$Fe_1$-NMC.

As a reference sample, sulfur loaded on plain NMC (S@NMC) was successfully prepared (Figure S20). Elemental mapping of S@NMC demonstrated that sulfur is well distributed on the carbon walls. XRD patterns of S@$Fe_1$-NMC and S@-NMC are shown in Figure S21, in which the peaks are indexed to crystalline sulfur (JCPDF 42-1278). Interestingly, the XRD results suggest that the dominant component of these two samples is sulfur, and the absence of Fe peaks in S@$Fe_1$-NMC could be attributed to its atomic dispersion. Thermogravimetric analysis (TGA) of S@$Fe_1$-NMC and S@-NMC indicates that the sulfur in the two samples is about 69 and 62 wt %, respectively (Figure S22). The greater S loading ratio in S@$Fe_1$-NMC demonstrates that atomically dispersed Fe is favorable for the capture of sulfur and improvement of its loading.

X-ray absorption near-edge structure (XANES) and extended X-ray absorption fine structure (EXAFS) measurements were employed to investigate the coordination environment and chemical states of S@$Fe_1$-NMC and $Fe_1$-NMC. Figure 3A presents the Fe K-edge XANES spectra of S@$Fe_1$-NMC, $Fe_1$-NMC, FeO, $Fe_2O_3$, and Fe foil.

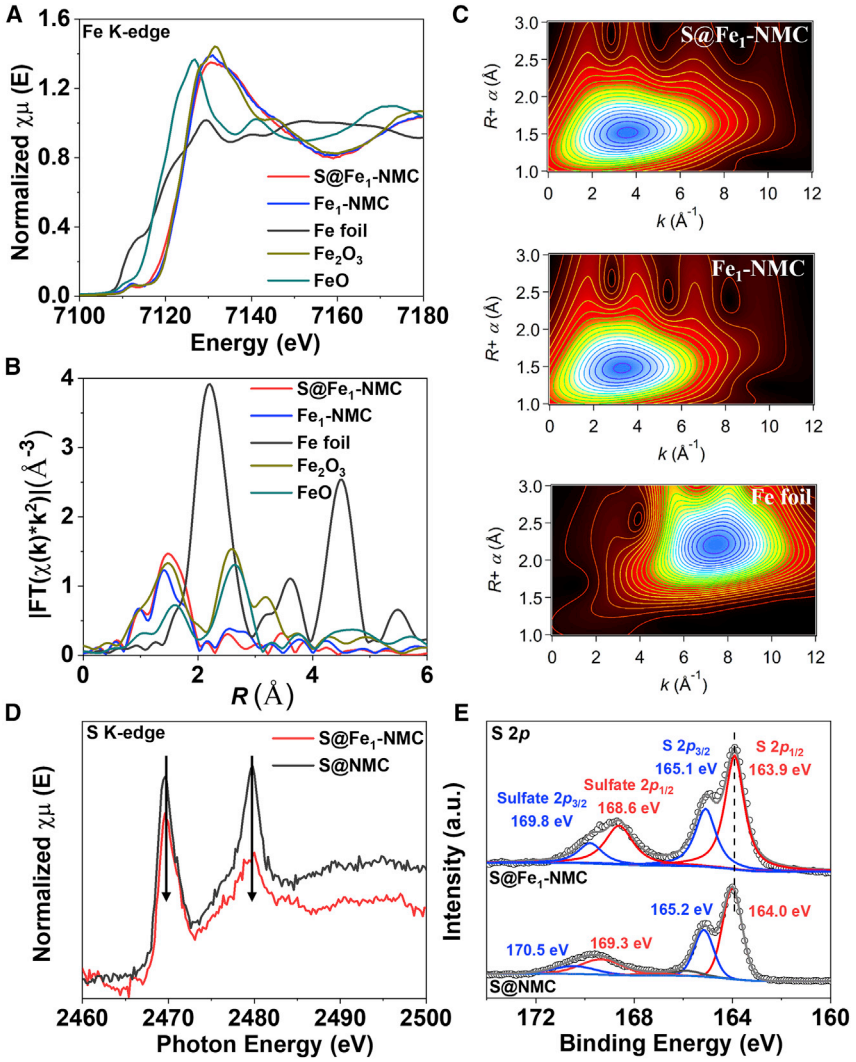


**Figure 3. X-ray absorption fine structure analyses**

(A and B) Fe K-edge XANES spectra (A) and R-space EXAFS spectra (B) of S@$Fe_1$-NMC, $Fe_1$-NMC, Fe foil, $Fe_2O_3$, and FeO.

(C) Wavelet transforms for the $k^3$ S@$Fe_1$-NMC, $Fe_1$-NMC, and Fe foil spectra with optimum resolution at 2.0 Å.

(D and E) S K-edge NEXAFS spectra (D) and S 2p region of the XPS spectra (E) for S@$Fe_1$-NMC and S@-NMC.

The intensities of $Fe_1$-NMC and S@$Fe_1$-NMC are greater than that of Fe foil and close to those of FeO and $Fe_2O_3$, suggesting that the Fe in $Fe_1$-NMC and S@$Fe_1$-NMC is in an oxidation state. In addition, the first-derivative XANES peaks for $Fe_1$-NMC and S@$Fe_1$-NMC are located at the position of $Fe_2O_3$, indicating that their stable valence states are approximately +3. The white line intensity of S@$Fe_1$-NMC is lower than that of $Fe_1$-NMC, indicating that the encapsulated S would be adsorbed on single Fe atoms, leading to the formation of S-Fe chemical bonds. The EXAFS Fourier transform (FT) of S@$Fe_1$-NMC and $Fe_1$-NMC shows no obvious peak for Fe-Fe bonds around 2.21 Å, thereby excluding the possibility of aggregation of Fe atoms (Figure 3B; Figure S23). $Fe_1$-NMC has a major peak at 1.41 Å, which is assumed result from the Fe-$N_4$ structure.[46] The prominent peak at 1.47 Å in S@$Fe_1$-NMC is attributed to the adsorption of sulfur, that is, the formation of the S-Fe-$N_4$ structure

(corresponding to the DFT results). EXAFS wavelet transform (WT), which simultaneously provides radial distance resolution and k-space resolution, is a useful tool to discriminate the backscattering atoms, even if they overlap in R-space.[47] The WT analysis of $Fe_1$-NMC (Figure 3C) presents an intensity maximum at 3.36 $Å^{-1}$, which can be attributed to the Fe-N/carbon (C) contributions originating from the mononuclear Fe centers without an Fe-derived crystalline structure in $Fe_1$-NMC. Moreover, the intensity maximum at 3.63 $Å^{-1}$ in S@$Fe_1$-NMC demonstrates the S-Fe-N/C structure.[46]

Near-edge X-ray absorption fine structure (NEXAFS) spectra of these two S hosts (Figure 3D; Figure S24) were collected to investigate the electron transfer behavior of sulfur. The decreased intensity of the S K-edge in S@$Fe_1$-NMC compared with that of S@NMC implies electron transfer from Fe-$N_4$ to S,[28] consistent with the DFT prediction. X-ray photoelectron spectra (XPSs) of the two samples are shown in Figure 3E and in Figures S25 and S26. The S 2p XPS of S@$Fe_1$-NMC can be separated into $2p_{3/2}$ (163.9 eV) and $2p_{1/2}$ (165.1 eV). The S $2p_{3/2}$ XPS peak is left shifted by 0.1 eV compared with that of S@NMC ($2p_{3/2}$: 164.0 eV). This negative shift can be assumed result from chemical coupling between S and $Fe_1$-NMC via electron transfer. The Fe-N structure can be found in the N 1 s XPS of S@$Fe_1$-NMC. In addition, the negative shift of 0.6 eV of C-N in S@$Fe_1$-NMC compared with S@NMC demonstrates the existence of S-Fe-$N_4$ sites.

## Electrochemical performance of Na-S batteries

The discharge/charge profiles of the $1^{st}$, $2^{nd}$, $10^{th}$, $100^{th}$, $300^{th}$, and $500^{th}$ cycles at 100 mA $g^{-1}$ for S@$Fe_1$-NMC and S@NMC cathode materials are presented in Figure 4A and Figure S27. The RT-Na/S@$Fe_1$-NMC battery presents two long plateaus from 1.6 to 1.2 V and from 1.2 to 0.8 V during the first discharge process, which is assumed to relate to the transformation of solid sulfur into sodium polysulfides and further sodiation to short-chain sulfides, respectively. The RT-Na/S@NMC cell showed a high plateau for the solid-liquid transition at 2.16 V. The lower potential plateau of S@$Fe_1$-NMC suggests that additional energy is required to break up the S-Fe-$N_4$ structure in S@$Fe_1$-NMC. Consequently, the subsequent discharge potential plateaus showed positive shifts[9] without the S-Fe-$N_4$ structure, whereas the subsequent plateaus of S@NMC shifted to the negative direction. The S@$Fe_1$-NMC cathode delivered a high initial capacity of 1,650 mAh $g^{-1}$, close to the theoretical capacity of sulfur, which is about 2.4 times greater than that of S@NMC (686 mAh $g^{-1}$). The $1^{st}$ discharge capacity of S@$Fe_1$-NMC (2,395 mAh $g^{-1}$) is higher than the theoretical capacity of sulfur (1,675 mAh $g^{-1}$), which could be attributed to the formation of solid-electrolyte interphase (SEI) and side reactions.[48] This high capacity could occur because the S-Fe-$N_4$ sites can enhance the reactivity and improve the kinetic conversion of polysulfides simultaneously. The electrochemical impedance spectra (EISs) of these two samples (Figure 4B) showed that S@$Fe_1$-NMC possesses a lower resistance, because the Fe-$N_4$ structure in S@$Fe_1$-NMC can transfer the electron to sulfur, thus enhancing its conductivity. The plateaus of S@$Fe_1$-NMC are not obvious, likely for two main reasons. The first is the electron transfer behavior of sulfur. The EXAFS and NEXAFS results (Figure 2) demonstrated that the electron of Fe-$N_4$ sites could transfer to sulfur, which could improve the reactivity of sulfur. This electron donor/acceptor will affect the reaction of sulfur with sodium. Second, the Fe-$N_4$ sites could cause rapid electrocatalytic reduction of polysulfides into the final product of $Na_2S$. These two reasons result in the plateaus not appearing.

The long-term cycling stability of S@$Fe_1$-NMC and S@NMC cathodes is shown in Figure 4C over 500 cycles at 0.1 mA $g^{-1}$. S@$Fe_1$-NMC presented an excellent

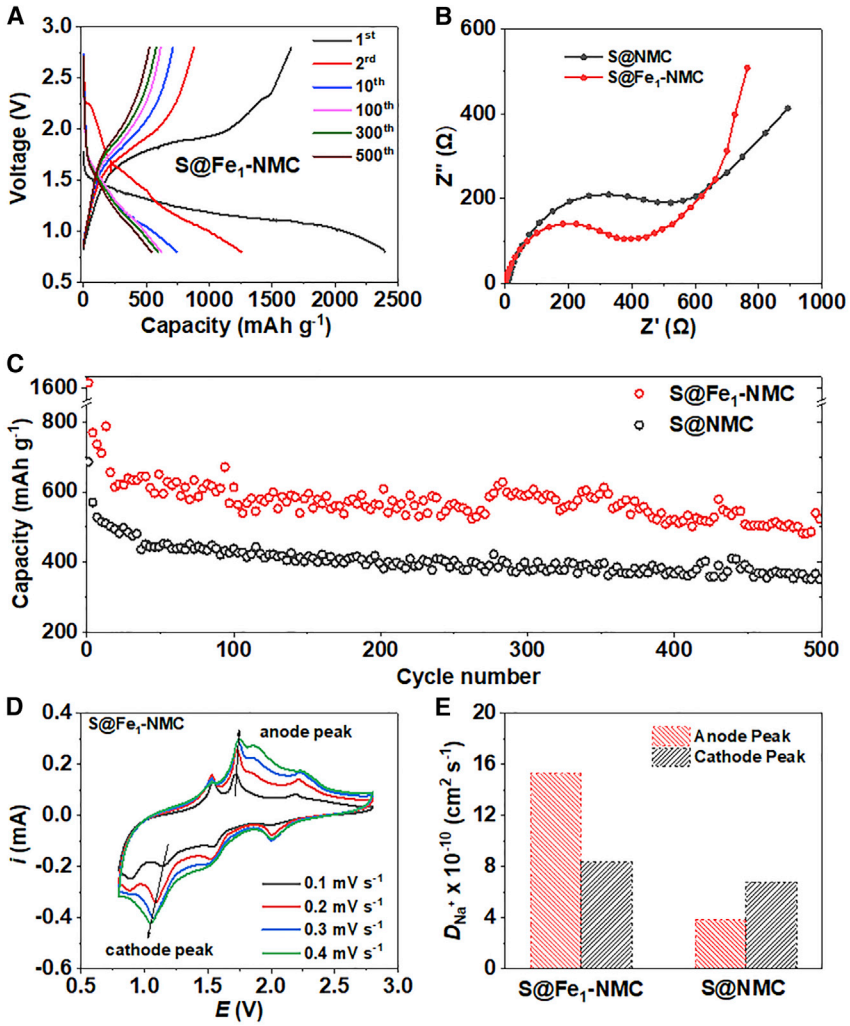


**Figure 4. Electrochemical performance of RT-Na/S batteries**

(A) Discharge/charge curves for selected cycles of S@$Fe_1$-NMC.

(B) Nyquist plots for S@$Fe_1$-NMC and S@-NMC.

(C) Cycling performance for S@$Fe_1$-NMC and S@-NMC.

(D) CV curves of S@$Fe_1$-NMC at various scan speeds from 0.1 to 0.4 mV $s^{-1}$.

(E) $Na^+$ diffusion coefficients of S@$Fe_1$-NMC and S@NMC.

reversible capacity of 540 mAh $g^{-1}$ after 500 cycles; in contrast, the S@NMC cathodes delivered a capacity of 351 mAh $g^{-1}$. The Coulomb efficiencies (CEs) of S@NMC and S@$Fe_1$-NMC are shown in Figure S28C. It can be seen that the first CE of S@$Fe_1$-NMC is 68.9%, which is higher than that of S@NMC (43.6%). The greater first CE also suggested high activity of S in S@$Fe_1$-NMC because of the electron transfer. The greater stability of S@$Fe_1$-NMC likely originates from the efficient sites provided by single Fe atoms for the adsorption of sodium polysulfides, thus preventing the dissolution of long-chain polysulfides. The rate performance at various current densities from 0.1 to 2 A $g^{-1}$ of these two samples is shown in Figure S28. S@$Fe_1$-NMC exhibits reversible capabilities of 730, 588, 498, 360, and 258 mAh $g^{-1}$ at 0.1, 0.2, 0.5, 1, and 2 A $g^{-1}$, respectively, which are higher than those of S@NMC. When the initial current density of 0.1 A $g^{-1}$ is resumed, a higher reversible capacity of 560 mAh $g^{-1}$ over 150 cycles can be obtained by the S@$Fe_1$-NMC

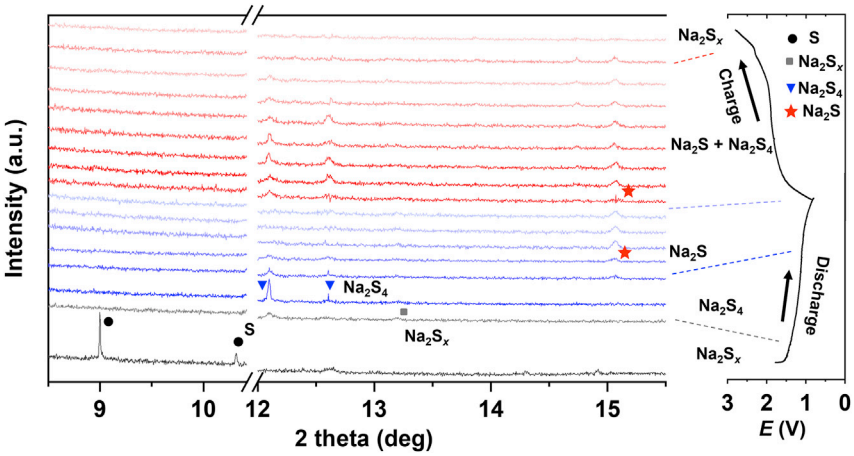


**Figure 5. *In situ* synchrotron XRD results**

*In situ* synchrotron XRD results of S@$Fe_1$-NMC cells (left) with the initial galvanostatic charge/discharge curves (right) at 100 mA $g^{-1}$.

cathode compared with that of S@NMC (319 mAh $g^{-1}$). The long cycle performance of S@$Fe_1$-NMC at a large current density (0.84 A $g^{-1}$) is shown in Figure S29, which presents a high reversible capacity of 204 mAh $g^{-1}$ over 170 cycles. This outstanding performance of S@$Fe_1$-NMC can be attributed to the S-Fe-$N_4$ sites of S@$Fe_1$-NMC not only accelerating $Na^+$ diffusion but also supporting the catalytic conversion of reaction intermediates into $Na_2S$.

To investigate the kinetics of intermediate production, cyclic voltammograms (CVs) at various scan rates (v) for S@$Fe_1$-NMC and S@NMC were collected and are shown in Figure 4D and in Figures S30 and S31. We chose the obvious cathodic and anode scan peaks for scan speeds that varied between 0.1 and 0.4 mV $s^{-1}$, respectively, to study the $Na^+$ ion diffusion coefficient ($D_{Na}$). The $D_{Na}$ of these two cathodes was investigated using the Randles-Sevcik equation. The linear relationship of the peak current ($I_p$) and $v^{0.5}$ was used to evaluate $D_{Na}$ for oxidation and reduction peaks.[49,50] Both the anode peak (A) and the cathode peak (C) of S@$Fe_1$-NMC are greater than those of S@NMC, suggesting higher electron and ionic transport than the latter during cycling. The $D_{Na}$ comparison of these two cathodes is shown in Figure 4E. For S@$Fe_1$-NMC, the anode peak of $D_{Na}$ is $1.52 \times 10^{-9}$ $cm^2$ $s^{-1}$, which is 4 times that of S@NMC ($3.80 \times 10^{-10}$ $cm^2$ $s^{-1}$); the cathodic peak of $D_{Na}$ for S@$Fe_1$-NMC is $8.37 \times 10^{-10}$ $cm^2$ $s^{-1}$ is also greater than that of S@NMC ($6.81 \times 10^{-10}$ $cm^2$ $s^{-1}$). The galvanostatic intermittent titration technique (GITT)'s second curves of S@$Fe_1$-NMC and S@-NMC at the current density of 0.5 A $g^{-1}$ (Figure S32) also show that the $Na^+$ ion diffusion coefficients of S@$Fe_1$-NMC are higher than those of S@NMC, suggesting that the S-Fe-$N_4$ sites will improve $Na^+$ ion diffusion. This result corroborates the DFT calculations and verifies the essential effect of S-Fe-$N_4$ sites on promoting Na diffusion.

*In situ* synchrotron XRD (l = 0.5904 Å) was also employed to demonstrate the enhanced kinetics (Figure 5). The initial peaks at 9.01° and 10.31° can be attributed to the (222) and (206) planes of S (JCPDF 42-1278). Then, two new peaks around 12.09° and 13.20° evolved upon discharged to 1.6 V, which can be indexed to the formation of $Na_2S_4$ and long-chain polysulfides ($Na_2S_x$), respectively. The coexistence of $Na_2S_x$ and $Na_2S_4$ suggests the fast kinetics of the S@$Fe_1$-NMC cell. When further discharged to 1.4 V, the intensities of the $Na_2S_4$ peaks at 12.09° and

12.60°, ascribed to the (213) and (312) planes of $Na_2S_4$ (JCPDF 25-1112), reached their maximum and then decreased. A new peak at 15.04° arose for S@$Fe_1$-NMC discharged to 0.8 V, which can be attributed to the (110) planes of $Na_2S$ (JCPDF 27-0793). The absence of the $Na_2S_2$ signal in the synchrotron XRD indicated that $Na_2S_4$ is rapidly reduced into $Na_2S$, substantiating that the Fe-$N_4$ sites will enhance the kinetic conversion of intermediates in RT-Na/S batteries. When the S@$Fe_1$-NMC cell is charged back to 2.8 V, $Na_2S_4$ is also detectable, indicating that the process from $Na_2S_4$ to $Na_2S$ is reversible. Meanwhile, the $Na_2S$ peak disappears when the voltage reaches 2.8 V, suggesting that $Na_2S$ was totally oxidized into $Na_2S_4$ and then $Na_2S_x$, corresponding to the high initial capacity of 1,650 mAh $g^{-1}$.

## EXPERIMENTAL PROCEDURES

### Resource availability

#### *Lead contact*

Further information and requests for resources and reagents should be directed to and will be fulfilled by the lead contact, Shu-Lei Chou (shulei@uow.edu.au).

#### *Materials availability*

This study did not generate new unique materials.

#### *Data and code availability*

The calculation code and experimental data generated during this study are available from the lead contact upon request.

### Density functional theory calculations

All calculations were performed using the plane-wave-based DFT method as implemented in the Vienna *ab initio* simulation package (VASP).[51,52] Projector augmented-wave pseudopotentials[53,54] with the generalized gradient approximation of the Perdew-Burke-Ernzerhof (PBE) exchange-correlation functional[55] were employed. An energy cutoff of 520 eV was adopted, and a k-point sampling of 2 × 2 × 1 in the Monkhorst-Pack scheme[56] was found to be sufficient for energy convergence. All structures were relaxed until a force tolerance of 0.02 eV/Å was reached. To complement the deficiencies of DFT in dealing with dispersion interactions, DFT-D3 semi-empirical van der Waals corrections[57] were applied for the structural optimization. A graphene supercell with a surface periodicity of 6 × 6 was taken as the basis for the construction of Fe-pyridine-$N_4$, graphitic N, and pyridinic $N_4$ moieties. A vacuum space of at least 15 Å in the z direction was used to avoid mirror interactions. The ΔG reaction energies of $Na_2S_x$ ($2 \leq x \leq 8$) with $Na^+/e^-$ pairs were calculated as follows:

$$\Delta G[Na_2S_x \rightarrow Na_{2+n}S_x] = E[Na_{2+n}S_x] - E[Na_2S_x] - nE[Na]$$

where $E[Na_2S_x]$ and $E[Na_{2+n}S_x]$ are the total energies of the configurations before and after sodiation, n (n = 1 or 2) is the number of $Na^+/e^-$ pairs, and E[Na] is the total energy of a single Na atom in its ground state (Na metal).

### Synthesis of NMC

Typically, 0.15 g of the $SiO_2$ nanoparticles (~100 nm) obtained earlier and 0.225 g of cetyltrimethylammonium bromide (CTAB) were added to a solution of deionized water (75 mL), ethanol (45 mL), and ammonia (0.825 mL, 28 wt %). The mixture became a homogeneously dispersed solution after treatment with ultrasound and stirring, for 30 min each, and then 0.12 mL of tetraethyl orthosilicate (TEOS) was injected. The reaction was allowed to proceed for 6 h at 25°C under gentle stirring. The products were collected by centrifugation, washed with ethanol, and redispersed into 60 mL

of $NH_4NO_3$/ethanol (6 g/L) solution to remove the CTAB surfactant. This extraction process proceeded at 60°C for 10 h to yield core-shell $SiO_2$@mesoporous silica ($mSiO_2$, with a thickness of ~15 nm) nanoparticles. Then, the $SiO_2$@$mSiO_2$ particles were used as hard templates. They were first coated with resorcinol formaldehyde (RF) via a sol-gel process. Specifically, 0.15 g of $SiO_2$@$mSiO_2$ and 0.46 g of CTAB were added into 14.08 mL of $H_2O$ and transferred into a three-neck, round-bottom flask. Homogeneous dispersion could be obtained after continuous ultrasonication and stirring for 0.5 h. Second, 0.7 g of resorcinol, 56.4 mL of absolute ethanol, and 0.2 mL of $NH_4OH$ were added into the dispersion sequentially, and the flask was maintained at 35°C with stirring for 0.5 h, followed by the addition of 0.1 mL of formalin. The RF polymerization could be completed after continually stirring for 6 h at 35°C and aging overnight. The obtained $SiO_2$@$mSiO_2$@RF nanospheres were collected and washed with deionized water and alcohol. The core-shell $SiO_2$@$mSiO_2$@C sample was prepared by calcination of the $SiO_2$@$mSiO_2$@RF powder at 800°C for 4 h (5°C $min^{-1}$) in a $NH_3$ atmosphere. Finally, NMC was prepared by etching away the $SiO_2$@$mSiO_2$ template with a 2.0 M NaOH solution.

### Synthesis of $Fe_1$-NMC

$Fe_1$-NMC was prepared through dispersion of 6.2 mg of $FeCl_2$ and 50 mg of NMC in Millipore water (18.2 MΩ·cm) under ultrasonication for 30 min (ultrasonic bath, 480 W; Bandelin Electronic). The resultant mixture was freeze-dried (Alpha 1-2 LDplus Entry Freeze Dryer, Refrigeration system, 0.43 kW; Martin Christ) for 48 h to remove water, followed by thermal treatment at 300°C for 2 h in 5 vol % $H_2$ in $N_2$, forming Fe nanoparticles (Fe NPs/NMC). The resultant powders were leached in 2 M HCl for 24 h and then 2 M $HNO_3$ for 24 h. Finally, the sample was collected by centrifugation and washed with water and ethanol several times. The electrocatalyst thus produced was designated $Fe_1$-NMC. The inductively coupled plasma (ICP)-optical emission spectroscopy (OES) results demonstrated that the Fe mass loading of $Fe_1$-NMC was ~1.0%.

### Synthesis of sulfur cathode samples

A mixture of $Fe_1$-NMC:S with a weight ratio of 1:3 was sealed in a quartz ampoule and thermally treated at 300°C for 2 h in a $N_2$ atmosphere. This new sample was denoted as S@$Fe_1$-NMC. In addition, a reference sample with plain NMC as the S host was prepared, in which S was embedded into the plain NMC framework (denoted as S@NMC). The synthesis procedures were the same as those for S@$Fe_1$-NMC but with NMC used instead of $Fe_1$-NMC.

### Characterization

The morphologies of the samples were investigated by transmission electron microscopy (TEM) (JEOL 2011, 200 keV) and STEM (JEOL ARM-200F, 200 keV). The XRD patterns were collected on a powder XRD (GBC MMA diffractometer) with Cu Kα radiation at a scan rate of 1° $min^{-1}$. XPS measurements were carried out using Al Kα radiation and fixed analyzer transmission mode: the pass energy was 60 eV for the survey spectra and 20 eV for the specific elements. The X-ray absorption spectra at the Fe K-edge were recorded at the X-ray absorption spectroscopy (XAS) station of the Beijing Synchrotron Radiation Facility (BSRF). The data collection was carried out in transmission mode for the Fe K-edge X-ray absorption fine structure (XAFS). All spectra were collected under ambient conditions.

### Electrochemical measurements

The electrochemical tests were conducted by assembling coin-type half-cells in an argon-filled glove box. The slurry was prepared by fully mixing 70 wt % active

materials (S@$Fe_1$-NMC and S@NMC), 10 wt % carbon black, and 20 wt % carboxymethyl cellulose (CMC) in an appropriate amount of water via a planetary mixer (KK-250S). Then, the obtained slurry was pasted on Cu foil using a doctor blade with a thickness of 100 μm, which was followed by drying at 50°C in a vacuum oven overnight. The mass loading of active materials of S@$Fe_1$-NMC and S@NMC was around 1.0 mg $cm^{-2}$. The capacities of cells in this work were normalized based on the mass of sulfur. The working electrode was prepared by punching the electrode film into discs 0.97 cm in diameter. Sodium foil was employed as both reference and counter electrode. The electrodes were separated by a glass fiber separator. The electrolyte consisted of 1.0 M $NaClO_4$ in propylene carbonate/ethylene carbonate with a volume ratio of 1:1 and 5 wt % fluoroethylene carbonate additive (PC/EC + 5 wt % FEC). The electrochemical performance was tested on a Land Battery Tester with a voltage window of 0.8–2.8 V. All capacities of cells have been normalized based on the weight of sulfur. Cyclic voltammetry was performed using a Biologic VMP-3 electrochemical workstation.

For *in situ* synchrotron XRD measurements, the cells were similar to the previously mentioned coin cells for electrochemical performance testing. To enhance the diffraction peak intensity, a thicker layer of cathode material was loaded on the Cu foil, with loading up to 5 mg $cm^{-2}$. To guarantee that the X-ray beams could penetrate the whole cell and that the electrochemical reactions could be monitored, three 4-mm-diameter holes were punched in the negative and positive caps, as well as the spacer. Then, Kapton film (only showing low-intensity responses in XRD patterns) was used to cover the holes in the negative and positive caps, and AB glue was used for complete sealing. The charge/discharge process was conducted with a battery test system (Neware) that was connected to the cell.

The $D_{Na}$ of these two cathodes were investigated using the Randles-Sevcik equation, as shown below:

$$I_p = 2.69 \times 10^5 n^{1.5} A D_{Na}{}^{0.5} v^{0.5} C_{Na}$$

where $I_p$ is the peak current (in amperes), n indicates the number of electrons in the reaction, A represents the electrode areas (per square centimeter), v is the scan speed (in volts per second), and $C_{Na}$ is the Na concentration in the electrolyte (in moles per cubic centimeter).

## SUPPLEMENTAL INFORMATION

Supplemental information can be found online at https://doi.org/10.1016/j.xcrp.2021.100531.

## ACKNOWLEDGMENTS

This research was supported by the Australian Research Council (ARC) (DE170100928, DP200100365, FT180100585, and LP180100722), the Commonwealth of Australia through the Automotive Australia 2020 Cooperative Research Centre (Auto CRC), National Natural Science Foundation of China (grant no. 51971124), and a Shenzhen Science and Technology research grant (ZDSYS201707281026184). The authors acknowledge Dr. Tania Silver for her critical reading.

## AUTHOR CONTRIBUTIONS

B.-W.Z., L.C., Y.-X.W., F.P., and S.-L.C. conceived and designed the experiments. B.-W.Z. and H.-L.Y. performed all synthetic and characterization experiments. S.L. and X.L. performed DFT simulations. W.-H.L. performed XRD experiments. S.Z., J.D.,

Y.D., and S.-Q.C. performed the XAS experiments. B.-W.Z. and Q.-F.G. performed synchrotron X-ray diffraction measurements. B.-W.Z., L.C., Y.-X.W., J.L., X.X., S.-L.C., H.-K.L., and S.-X.D. analyzed the data and wrote the manuscript. All authors read and approved the final manuscript.

## DECLARATION OF INTERESTS

The authors declare no competing interests.

Received: January 25, 2021
Revised: June 21, 2021
Accepted: July 16, 2021
Published: August 6, 2021

## REFERENCES

1. Yang, X., Luo, J., and Sun, X. (2020). Towards high-performance solid-state Li-S batteries: from fundamental understanding to engineering design. Chem. Soc. Rev. *49*, 2140–2195.

2. Pang, Q., Shyamsunder, A., Narayanan, B., Kwok, C.Y., Curtiss, L.A., and Nazar, L.F. (2018). Tuning the electrolyte network structure to invoke quasi-solid state sulfur conversion and suppress lithium dendrite formation in Li-S batteries. Nat. Energy *3*, 783–791.

3. Liu, H., Pei, W., Lai, W.H., Yan, Z., Yang, H., Lei, Y., Wang, Y.X., Gu, Q., Zhou, S., Chou, S., et al. (2020). Electrocatalyzing S Cathodes *via* Multisulfiphilic Sites for Superior Room-Temperature Sodium-Sulfur Batteries. ACS Nano *14*, 7259–7268.

4. Chung, S.-H., and Manthiram, A. (2019). Current Status and Future Prospects of Metal-Sulfur Batteries. Adv. Mater. *31*, e1901125.

5. Zhao, M., Peng, H.-J., Zhang, Z.-W., Li, B.-Q., Chen, X., Xie, J., Chen, X., Wei, J.-Y., Zhang, Q., and Huang, J.-Q. (2019). Activating Inert Metallic Compounds for High-Rate Lithium-Sulfur Batteries Through *In Situ* Etching of Extrinsic Metal. Angew. Chem. Int. Ed. Engl. *58*, 3779–3783.

6. Chen, B., Wang, T., Zhao, S., Tan, J., Zhao, N., Jiang, S.P., Zhang, Q., Zhou, G., and Cheng, H.M. (2021). Efficient Reversible Conversion between $MoS_2$ and Mo/$Na_2S$ Enabled by Graphene-Supported Single Atom Catalysts. Adv. Mater. *33*, 2007090.

7. Wang, R., Yang, J.L., Chen, X., Zhao, Y., Zhao, W.G., Qian, G.Y., Li, S.N., Xiao, Y.G., Chen, H., Ye, Y.S., et al. (2020). Highly Dispersed Cobalt Clusters in Nitrogen-Doped Porous Carbon Enable Multiple Effects for High-Performance Li-S Battery. Adv. Energy Mater. *10*, 1903550.

8. Zhao, Y., Tan, R., Yang, J., Wang, K., Gao, R., Liu, D., Liu, Y.D., Yang, J.L., and Pan, F. (2017). 3D-hybrid material design with electron/lithium-ion dual-conductivity for high-performance Li-sulfur batteries. J. Power Sources *340*, 160–166.

9. Zhang, B.W., Sheng, T., Liu, Y.D., Wang, Y.X., Zhang, L., Lai, W.H., Wang, L., Yang, J., Gu, Q.F., Chou, S.L., et al. (2018). Atomic cobalt as an efficient electrocatalyst in sulfur cathodes for superior room-temperature sodium-sulfur batteries. Nat. Commun. *9*, 4082.

10. Lu, Q., Wang, X., Cao, J., Chen, C., Chen, K., Zhao, Z., Niu, Z., and Chen, J. (2017). Freestanding carbon fiber cloth/sulfur composites for flexible room-temperature sodium-sulfur batteries. Energy Storage Mater. *8*, 77–84.

11. Xu, X., Zhou, D., Qin, X., Lin, K., Kang, F., Li, B., Shanmukaraj, D., Rojo, T., Armand, M., and Wang, G. (2018). A room-temperature sodium-sulfur battery with high capacity and stable cycling performance. Nat. Commun. *9*, 3870.

12. Yang, H., Zhang, B., Wang, Y.X., Konstantinov, K., Liu, H.K., and Dou, S.X. (2020). Alkali-Metal Sulfide as Cathodes toward Safe and High-Capacity Metal (M = Li, Na, K). Sulfur Batteries. Adv. Energy Mater. *10*, 2001764.

13. Chen, H., Zhou, G., Boyle, D., Wan, J., Wang, H., Lin, D., Mackanic, D., Zhang, Z., Kim, S.C., Lee, H.R., et al. (2020). Electrode Design with Integration of High Tortuosity and Sulfur-Philicity for High-Performance Lithium-Sulfur Battery. Matter *2*, 1605–1620.

14. Wang, Y.X., Zhang, B., Lai, W., Xu, Y., Chou, S.L., Liu, H.K., and Dou, S.X. (2017). Room-Temperature Sodium-Sulfur Batteries: A Comprehensive Review on Research Progress and Cell Chemistry. Adv. Energy Mater. *7*, 1602829.

15. Yang, H., Xu, H., Li, M., Zhang, L., Huang, Y., and Hu, X. (2016). Assembly of NiO/Ni(OH)2/PEDOT Nanocomposites on Contra Wires for Fiber-Shaped Flexible Asymmetric Supercapacitors. ACS Appl. Mater. Interfaces *8*, 1774–1779.

16. Li, B.Q., Zhang, S.Y., Kong, L., Peng, H.J., and Zhang, Q. (2018). Porphyrin Organic Framework Hollow Spheres and Their Applications in Lithium-Sulfur Batteries. Adv. Mater. *30*, e1707483.

17. Wei, S., Ma, L., Hendrickson, K.E., Tu, Z., and Archer, L.A. (2015). Metal-Sulfur Battery Cathodes Based on PAN-Sulfur Composites. J. Am. Chem. Soc. *137*, 12143–12152.

18. Wang, Y.X., Yang, J., Lai, W., Chou, S.L., Gu, Q.F., Liu, H.K., Zhao, D., and Dou, S.X. (2016). Achieving High-Performance Room-Temperature Sodium-Sulfur Batteries With S@Interconnected Mesoporous Carbon Hollow Nanospheres. J. Am. Chem. Soc. *138*, 16576–16579.

19. Yu, X., and Manthiram, A. (2014). Room-Temperature Sodium-Sulfur Batteries with Liquid-Phase Sodium Polysulfide Catholytes and Binder-Free Multiwall Carbon Nanotube Fabric Electrodes. J. Phys. Chem. C *118*, 22952–22959.

20. Xin, S., Yin, Y.X., Guo, Y.G., and Wan, L.J. (2014). A high-energy room-temperature sodium-sulfur battery. Adv. Mater. *26*, 1261–1265.

21. Zhang, B.W., Sheng, T., Wang, Y.X., Chou, S., Davey, K., Dou, S.X., and Qiao, S.Z. (2019). Long-Life Room-Temperature Sodium-Sulfur Batteries by Virtue of Transition-Metal-Nanocluster-Sulfur Interactions. Angew. Chem. Int. Ed. Engl. *58*, 1484–1488.

22. Zheng, S., Han, P., Han, Z., Li, P., Zhang, H., and Yang, J. (2014). Nano-Copper-Assisted Immobilization of Sulfur in High-Surface-Area Mesoporous Carbon Cathodes for Room Temperature Na-S Batteries. Adv. Energy Mater. *4*, 1400226.

23. Wang, N., Wang, Y., Bai, Z., Fang, Z., Zhang, X., Xu, Z., Ding, Y., Xu, X., Du, Y., Dou, S., et al. (2020). High-performance room-temperature sodium-sulfur battery enabled by electrocatalytic sodium polysulfides full conversion. Energy Environ. Sci. *13*, 562–570.

24. Yan, Z., Liang, Y., Xiao, J., Lai, W., Wang, W., Xia, Q., Wang, Y., Gu, Q., Lu, H., Chou, S.L., et al. (2020). A High-Kinetics Sulfur Cathode with a Highly Efficient Mechanism for Superior Room-Temperature Na-S Batteries. Adv. Mater. *32*, e1906700.

25. Zhou, G., Tian, H., Jin, Y., Tao, X., Liu, B., Zhang, R., Seh, Z.W., Zhuo, D., Liu, Y., Sun, J., et al. (2017). Catalytic oxidation of $Li_2S$ on the surface of metal sulfides for Li-S batteries. Proc. Natl. Acad. Sci. USA *114*, 840–845.

26. Li, P., Ma, L., Wu, T., Ye, H., Zhou, J., Zhao, F., Han, N., Wang, Y., Wu, Y., Li, Y., et al. (2018). Chemical Immobilization and Conversion of Active Polysulfides Directly by Copper Current Collector: A New Approach to Enabling Stable Room-Temperature Li-S and Na-S Batteries. Adv. Energy Mater. *8*, 1800624.

27. Ma, D., Li, Y., Yang, J., Mi, H., Luo, S., Deng, L., Yan, C., Rauf, M., Zhang, P., Sun, X., et al.

(2018). New Strategy for Polysulfide Protection Based on Atomic Layer Deposition of $TiO_2$ onto Ferroelectric-Encapsulated Cathode: Toward Ultrastable Free-Standing Room Temperature Sodium-Sulfur Batteries. Adv. Funct. Mater. *28*, 1705537.

28. Ye, C., Jiao, Y., Chao, D., Ling, T., Shan, J., Zhang, B., Gu, Q., Davey, K., Wang, H., and Qiao, S.Z. (2020). Electron-State Confinement of Polysulfides for Highly Stable Sodium-Sulfur Batteries. Adv. Mater. *32*, e1907557.

29. Zhou, D., Tang, X., Guo, X., Li, P., Shanmukaraj, D., Liu, H., Gao, X., Wang, Y., Rojo, T., Armand, M., and Wang, G. (2020). Polyolefin-Based Janus Separator for Rechargeable Sodium Batteries. Angew. Chem. Int. Ed. Engl. *59*, 16725–16734.

30. Yu, X., and Manthiram, A. (2016). Performance Enhancement and Mechanistic Studies of Room-Temperature Sodium-Sulfur Batteries with a Carbon-Coated Functional Nafion Separator and a $Na_2S$/Activated Carbon Nanofiber Cathode. Chem. Mater. *28*, 896–905.

31. Chen, B., Chao, D., Liu, E., Jaroniec, M., Zhao, N., and Qiao, S.Z. (2020). Transition metal dichalcogenides for alkali metal ion batteries: engineering strategies at the atomic level. Energy Environ. Sci. *13*, 1096–1131.

32. Zheng, X., Cui, P., Qian, Y., Zhao, G., Zheng, X., Xu, X., Cheng, Z., Liu, Y., Dou, S.X., and Sun, W. (2020). Multifunctional Active-Center-Transferable Platinum/Lithium Cobalt Oxide Heterostructured Electrocatalysts towards Superior Water Splitting. Angew. Chem. Int. Ed. Engl. *59*, 14533–14540.

33. Yang, H.B., Hung, S.F., Liu, S., Yuan, K., Miao, S., Zhang, L., Huang, X., Wang, H.-Y., Cai, W., Chen, R., et al. (2018). Atomically dispersed Ni(I) as the active site for electrochemical $CO_2$ reduction. Nat. Energy *3*, 140–147.

34. Zheng, S.S., Zuo, C.J., Liang, X.H., Li, S.N., and Pan, F. (2021). Valence state of transition metal center as an activity descriptor for $CO_2$ reduction on single atom catalysts. J. Energy. Chem *56*, 444–448.

35. Han, A., Chen, W., Zhang, S., Zhang, M., Han, Y., Zhang, J., Ji, S., Zheng, L., Wang, Y., Gu, L., et al. (2018). A Polymer Encapsulation Strategy to Synthesize Porous Nitrogen-Doped Carbon-Nanosphere-Supported Metal Isolated-Single-Atomic-Site Catalysts. Adv. Mater. *30*, e1706508.

36. Zhang, B.W., Wang, Y.X., Chou, S.L., Liu, H.K., and Dou, S.X. (2019). Fabrication of Superior Single-Atom Catalysts toward Diverse Electrochemical Reactions. Small Methods *3*, 1800497.

37. Lu, C., Fang, R., and Chen, X. (2020). Single-Atom Catalytic Materials for Advanced Battery Systems. Adv. Mater. *32*, e1906548.

38. Zhou, G., Zhao, S., Wang, T., Yang, S.Z., Johannessen, B., Chen, H., Liu, C., Ye, Y., Wu, Y., Peng, Y., et al. (2020). Theoretical Calculation Guided Design of Single-Atom Catalysts toward Fast Kinetic and Long-Life Li-S Batteries. Nano Lett. *20*, 1252–1261.

39. Wang, A., Li, J., and Zhang, T. (2018). Heterogeneous single-atom catalysis. Nat. Rev. Chem. *2*, 65–81.

40. Wang, M., Fan, L., Sun, X., Guan, B., Jiang, B., Wu, X., Tian, D., Sun, K., Qiu, Y., Yin, X., et al. (2020). Nitrogen-Doped $CoSe_2$ as a Bifunctional Catalyst for High Areal Capacity and Lean Electrolyte of Li-S Battery. ACS Energy Lett. *5*, 3041–3050.

41. Qiu, Y., Fan, L., Wang, M., Yin, X., Wu, X., Sun, X., Tian, D., Guan, B., Tang, D., and Zhang, N. (2020). Precise Synthesis of Fe-$N_2$ Sites with High Activity and Stability for Long-Life Lithium-Sulfur Batteries. ACS Nano *14*, 16105–16113.

42. Du, Z., Chen, X., Hu, W., Chuang, C., Xie, S., Hu, A., Yan, W., Kong, X., Wu, X., Ji, H., and Wan, L.J. (2019). Cobalt in Nitrogen-Doped Graphene as Single-Atom Catalyst for High-Sulfur Content Lithium-Sulfur Batteries. J. Am. Chem. Soc. *141*, 3977–3985.

43. Zhang, L., Liu, D., Muhammad, Z., Wan, F., Xie, W., Wang, Y., Song, L., Niu, Z., and Chen, J. (2019). Single Nickel Atoms on Nitrogen-Doped Graphene Enabling Enhanced Kinetics of Lithium-Sulfur Batteries. Adv. Mater. *31*, e1903955.

44. Fei, H., Dong, J., Chen, D., Hu, T., Duan, X., Shakir, I., Huang, Y., and Duan, X. (2019). Single atom electrocatalysts supported on graphene or graphene-like carbons. Chem. Soc. Rev. *48*, 5207–5241.

45. Sun, Y.W., Liu, W., Hernandez, I., Gonzalez, J., Rodriguez, F., Dunstan, D.J., and Humphreys, C.J. (2019). 3D Strain in 2D Materials: To What Extent is Monolayer Graphene Graphite? Phys. Rev. Lett. *123*, 135501.

46. Fei, H., Dong, J., Feng, Y., Allen, C.S., Wan, C., Volosskiy, B., Li, M., Zhao, Z., Wang, Y., Sun, H., et al. (2018). General synthesis and definitive structural identification of MN4C4 single-atom catalysts with tunable electrocatalytic activities. Nat. Catal. *1*, 63–72.

47. Xia, Z., Zhang, H., Shen, K., Qu, Y., and Jiang, Z. (2018). Wavelet analysis of extended X-ray absorption fine structure data: Theory, application. Physica B *2018*, 12–19.

48. Zhang, B.W., Liu, Y.D., Wang, Y.X., Zhang, L., Chen, M.Z., Lai, W.H., Chou, S.L., Liu, H.K., and Dou, S.X. (2017). *In Situ* Grown S Nanosheets on Cu Foam: An Ultrahigh Electroactive Cathode for Room-Temperature Na-S Batteries. ACS Appl. Mater. Interfaces *9*, 24446–24450.

49. Wang, L., Chen, X., Li, S., Yang, J., Sun, Y., Peng, L., Shan, B., and Xie, J. (2019). Effect of eutectic accelerator in selenium-doped sulfurized polyacrylonitrile for high performance room temperature sodium-sulfur batteries. J. Mater. Chem. A Mater. Energy Sustain. *7*, 12732–12739.

50. Kim, H., Lee, J., Ahn, H., Kim, O., and Park, M.J. (2015). Synthesis of three-dimensionally interconnected sulfur-rich polymers for cathode materials of high-rate lithium-sulfur batteries. Nat. Commun. *6*, 7278.

51. Kresse, G., and Hafner, J. (1993). *Ab initio* molecular dynamics for liquid metals. Phys. Rev. B Condens. Matter *47*, 558–561.

52. Kresse, G., and Furthmüller, J. (1996). Efficient iterative schemes for *ab initio* total-energy calculations using a plane-wave basis set. Phys. Rev. B Condens. Matter *54*, 11169–11186.

53. Blöchl, P.E. (1994). Projector augmented-wave method. Phys. Rev. B Condens. Matter *50*, 17953–17979.

54. Kresse, G., and Joubert, D. (1999). Phys. Rev. B *59*, 1758–1775.

55. Perdew, J.P., Burke, K., and Ernzerhof, M. (1996). Generalized Gradient Approximation Made Simple. Phys. Rev. Lett. *77*, 3865–3868.

56. Monkhorst, H.J., and Pack, J.D. (1976). Special points for Brillouin-zone integrations. Phys. Rev. B Condens. Matter Mater. Phys. *13*, 5188–5192.

57. Grimme, S., Antony, J., Ehrlich, S., and Krieg, H. (2010). A consistent and accurate *ab initio* parametrization of density functional dispersion correction (DFT-D) for the 94 elements H-Pu. J. Chem. Phys. *132*, 154104.